THREE-DIMENSIONAL MICROMOTION SIGNATURE EXTRACTION OF ROTATING TARGETS IN OFDM-LFM MIMO RADAR

Ying Luo[1, 2], Qun Zhang[1, 2, *], Chengwei Qiu[3], Song Li[4], and Tat Soon Yeo[3]

[1]Institute of Information & Navigation, Air Force Engineering University, Xi'an 710077, China

[2]Key Laboratory for Information Science of Electromagnetic Waves (Ministry of Education), Fudan University, Shanghai 200433, China

[3]Departement of Electrical and Computer Engineering, National University of Singapore, Singapore 117576, Singapore

[4]Institute of Air and Missile Defense, Air Force Engineering University, Xi'an 710051, China

Abstract—In monostatic radars systems, only the micromotion signatures projected onto the radar line-of-sight (LOS) can be observed from echoes. As a result, the obtained micromotion signatures (e.g., the radius length of rotation) are sensitive to the radar LOS. In this paper, we propose a method for the accurate estimation of three-dimensional (3-D) micromotion signature with the orthogonal frequency division multiplexing — linear frequency modulation (OFDM-LFM) multi-input multi-output (MIMO) radar technique, which makes use of the advantages of the multi-view of MIMO radar systems and the broad bandwidth of the OFDM-LFM signals. In the proposed method, the Hough transform and Orthogonal Matching Pursuit (OMP) algorithm are introduced to extract the m-D curve features from echoes, and then the 3-D micromotion signatures of the rotating targets are obtained by solving nonlinear multivariable equation systems. The extracted 3-D micromotion signatures are no longer sensitive to the radar LOS, and can provide realistic feature information for target recognition. Simulations are given to validate the effectiveness of the proposed method.

1. INTRODUCTION

For radar target recognition applications, the micro-Doppler (m-D) signatures induced by the micromotion dynamics of a component or structure on a radar target can be regarded as unique signatures of the target and provide additional information for classification, recognition and identification of the object [1–5]. M-D effect is induced by the micromotion dynamics of radar targets, such as the spinning motion of a space target, rotors' rotation of a helicopter, wheels' rotation of a truck, vibration of a tank's surface. The m-D effect has attracted great research attention over the past decade. The high-resolution time-frequency transforms are utilized to analyze the m-D signatures in [1, 6–8]. The modified Hilbert-Huang transform, empirical-mode decomposition (EMD) and the Hough transform (HT) are developed to estimate the parameters of the rotating parts of target in [9–11]. The influences of target's micromotion on synthetic aperture radar (SAR) and ground moving target indication (GMTI) are discussed in [12, 13].

However, most of the existing research related to m-D effect has focused on the analysis and extraction of m-D signature in monostatic radar systems. In a monostatic radar system, only the micromotion signatures projected onto the line-of-sight (LOS) could be extracted from the target's echoes [1, 11, 14]. As a result, the obtained m-D signatures are sensitive to radar LOS. This kind of sensitivity increases the uncertainty in target recognition. Hence, a more effective approach is needed for obtaining the full micromotion signatures.

In recent years, the multi-input multi-output (MIMO) radar techniques attract increasing interests [15–18]. Studies show that MIMO radar system has many advantages, such as excellent interference rejection capability, improved parameter identifiability, increased diversity of the target information [15]. Moreover, the cross-range resolution of inverse synthetic aperture radar (ISAR) imaging of target in MIMO radar can be increased if the platforms are properly located [19, 20]. The ISAR imaging method in MIMO radar system is investigated in [21].

In our previous work [22], we put forward a concept of *three-dimensional (3-D) micro-Doppler* to describe the real micromotion phenomenon by means of the multi-view of MIMO radar. With the proposed concept of 3-D m-D, the real micromotion signatures, including radius and angular velocity vector of a rotating object, can be depicted exactly. In [22] we also presented a method of 3-D micromotion signature extraction for the narrowband MIMO radar. Due to the insufficient range resolution of the narrowband signal, we applied the time-frequency transforms to extract the

micromotion signatures. Nevertheless, when multiple m-D components coexist within a returned echo, the limit of the resolution capability of the time-frequency transforms would lead to low precision of the extracted micromotion signatures. Hence, in this paper, the orthogonal frequency division multiplexing — linear frequency modulation (OFDM-LFM) signal [23, 24] is employed to enhance the range resolution in order to improve the precision of extracted 3-D micromotion signatures. The orthogonal frequency division multiplexing (OFDM) scheme is one of the ways to accomplish simultaneous use of several subcarriers and illuminate target in different angles [23, 25]. Because the transmitted signals at each transmitter are wideband LFM pulses which guarantee high resolution of the radar system, thus, more accurate micromotion parameters could be obtained. Therefore, based on the OFDM-LFM MIMO radar system, we intend to propose a method for extracting the "realistic" 3-D micromotion signatures of rotating targets in the paper.

The paper is organized as follows. The m-D effect in OFDM-LFM MIMO radar induced by rotation is investigated in Section 2, and then the 3-D micromotion signature extraction method is proposed in Section 3. The simulations are given in Section 4, followed by some conclusions in the last section.

2. M-D EFFECT IN OFDM-LFM MIMO RADAR

In this section, we analyze the m-D effect in OFDM-LFM MIMO radar induced by rotation. To ensure non-interference between each two transmitters of the MIMO radar, the transmitted signals must be orthogonal to each other. Assuming the OFDM-LFM signals are transmitted by the MIMO radar, the transmitted signal of the mth transmitter is written as

$$s_m(t) = \text{rect}(t/T_p) \exp\left(j2\pi\left(f_c t + mkt/T_p + \mu t^2/2\right)\right),$$
$$m = 1, 2, \ldots, M; \quad k \in \mathbb{N} \tag{1}$$

where t is the fast-time, T_p the pulse duration, f_c the carrier frequency, μ the chirp rate, M the total number of transmitters in MIMO radar, k a natural number, $\mathbb{N}$ the set of all natural numbers, and $\text{rect}(t) = 1$ for $-1/2 \leq t \leq 1/2$ and zero otherwise. For the signals transmitted by the m_1th and m_2th transmitters, it can be calculated that

$$\int_{-T_p/2}^{T_p/2} s_{m_1}(t) s_{m_2}^*(t) dt = \begin{cases} T_p, & m_1 = m_2 \\ 0, & m_1 \neq m_2 \end{cases} \tag{2}$$

It is demonstrated that the transmitted signals between each two different transmitters are orthogonal to each other. In practice,

the operation frequency band of each two transmitters should not be overlapped to ensure the ideal orthogonality, i.e.,

$$k/T_p > c_1 \mu T_p, \quad c_1 > 1 \tag{3}$$

In the following, we assume the ideal orthogonality between each two transmitted signals for simplicity.

The geometry of the MIMO radar system and the target is shown in Fig. 1. $OXYZ$ is the global coordinate system and $oxyz$ the local coordinate system of the target with translations respect to the global coordinates. O_{T1}, O_{T2}, ..., O_{TM} denote the M transmitters, and O_{R1}, O_{R2}, ..., O_{RN} denote the N receivers. Assume that the target translates from $oxyz$ to $o'x'y'z'$ with velocity $\mathbf{v} = [v_X, v_Y, v_Z]^T$. Simultaneously, a scatterer P on the target rotates around the center C with angular velocity $\boldsymbol{\omega} = [\omega_x, \omega_y, \omega_z]^T$, where the superscript "T" means the transpose of a vector or a matrix. Let $\Omega = \|\boldsymbol{\omega}\|$. At the slow-time t_m, the received echo of the nth receiver from the scatterer P transmitted by the mth transmitter is written as

$$s_{m,n}(t, t_m) = \sigma_P(m, n) s_m(t - R_P(t_m; m, n)/c) \tag{4}$$

where $R_P(t_m; m, n)$ is the sum distance from P to the mth transmitter and the nth receiver at the slow-time t_m, and $\sigma_P(m, n)$ is the scattering coefficient of P. For simplicity, we assume that the translational motion between the target and radars can be compensated accurately. Therefore, the motion trajectory of the target is known, then the echoes from o can be chosen as the reference signals for the "dechirp"
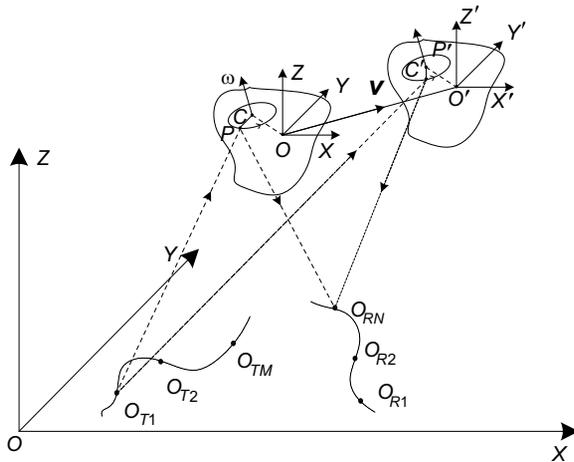
Figure 1. Geometry of a MIMO radar system and a rotating target.

processing [14, 26], i.e.,

$$s_{0m,n}(t, t_m) = s_m(t - R_0(t_m; m, n)/c) \tag{5}$$

where $R_0(t_m; m, n)$ is the sum distance from o to the mth transmitters and the nth receiver at slow-time t_m. After the "dechirp" processing, it yields

$$s_{dm,n}(t, t_m)$$
$$= \sigma_P(m, n)\text{rect}\left(\frac{t - R_P(t_m; m, n)/c}{T_p}\right) \times \exp\left(j2\pi\left(-\left(\frac{f_c}{c} + \frac{mk}{T_p c}\right)\right.\right.$$
$$\left.\left. R_\Delta(t_m; m, n) - \frac{\mu R_\Delta(t_m; m, n)}{c}t + \frac{\mu\left(R_P^2(t_m; m, n) - R_0^2(t_m; m, n)\right)}{2c^2}\right)\right) \tag{6}$$

where $R_\Delta(t_m; m, n) = R_P(t_m; m, n) - R_0(t_m; m, n)$. Taking the Fourier transform to $s_{dm,n}(t, t_m)$ with respect to t, and then removing the Residual Video Phase (RVP) [11], it yields

$$S_{m,n}(f, t_m) = \sigma_P(m, n) T_p \text{sinc}(T_p(f + \mu R_\Delta(t_m; m, n)/c))$$
$$\exp(-j2\pi(f_c/c + mk/(T_p c)) R_\Delta(t_m; m, n)) \tag{7}$$

It can be found that $|S_{m,n}(f, t_m)|$ is a sinc function which peaks at $f = -\mu R_\Delta(t_m; m, n)/c$. The range profile of the scatterer is then obtained, and the peak location is determined by the distance differential of $R_P(t_m; m, n)$ and $R_0(t_m; m, n)$.

Assume that the coordinates of O_{Tm} and O_{Rn} in the global coordinate system $OXYZ$ are (X_{Tm}, Y_{Tm}, Z_{Tm}) and (X_{Rn}, Y_{Rn}, Z_{Rn}) respectively, then it can be obtained according to the geometry shown in Fig. 1:

$$R_0(t_m; m, n) = \left\|\overrightarrow{O_{Tm}o} + \mathbf{v}t_m\right\| + \left\|\overrightarrow{O_{Rn}o} + \mathbf{v}t_m\right\|$$

$$= \sqrt{(X_o - X_{Tm} + v_X t_m)^2 + (Y_o - Y_{Tm} + v_Y t_m)^2 + (Z_o - Z_{Tm} + v_Z t_m)^2}$$
$$+ \sqrt{(X_o - X_{Rn} + v_X t_m)^2 + (Y_o - Y_{Rn} + v_Y t_m)^2 + (Z_o - Z_{Rn} + v_Z t_m)^2}$$

$$\approx R_0(0; m, n) + \left(\frac{(X_o - X_{Tm})v_X + (Y_o - Y_{Tm})v_Y + (Z_o - Z_{Tm})v_Z}{\sqrt{(X_o - X_{Tm})^2 + (Y_o - Y_{Tm})^2 + (Z_o - Z_{Tm})^2}}\right.$$

$$\left. + \frac{(X_o - X_{Rn})v_X + (Y_o - Y_{Rn})v_Y + (Z_o - Z_{Rn})v_Z}{\sqrt{(X_o - X_{Rn})^2 + (Y_o - Y_{Rn})^2 + (Z_o - Z_{Rn})^2}}\right) t_m \tag{8}$$

Let $R_C(t_m; m, n)$ be the sum distance from C' to the mth transmitter

and the nth receiver at slow-time t_m, then we have

$$R_C(t_m; m, n) = \left\|\overrightarrow{O_{Tm}o} + \overrightarrow{oC} + \mathbf{v}t_m\right\| + \left\|\overrightarrow{O_{Rn}o} + \overrightarrow{oC} + \mathbf{v}t_m\right\| \approx R_C(0; m, n)$$

$$+ \left(\frac{\frac{(X_o - X_{Tm} + x_C)v_X + (Y_o - Y_{Tm} + y_C)v_Y + (Z_o - Z_{Tm} + z_C)v_Z}{\sqrt{(X_o - X_{Tm} + x_C)^2 + (Y_o - Y_{Tm} + y_C)^2 + (Z_o - Z_{Tm} + z_C)^2}}}{+ \frac{(X_o - X_{Rn} + x_C)v_X + (Y_o - Y_{Rn} + y_C)v_Y + (Z_o - Z_{Rn} + z_C)v_Z}{\sqrt{(X_o - X_{Rn} + x_C)^2 + (Y_o - Y_{Rn} + y_C)^2 + (Z_o - Z_{Rn} + z_C)^2}}} \right) t_m \quad (9)$$

For calculating $R_\Delta(t_m; m, n)$, the geometry of the target and a pair of transmitter and receiver at t_m is simplified as shown in Fig. 2, where $\mathbf{n}_1$ and $\mathbf{n}_2$ denote the LOS vectors of the transmitter and receiver respectively, and P_1 and P_2 are the projections of P' on $\mathbf{n}_1$ and $\mathbf{n}_2$, respectively. During the imaging interval, $\mathbf{n}_1$ and $\mathbf{n}_2$ can be regarded invariable. For $||\overline{C'P'}|| \ll ||\overline{O_{Tm}C'}||$ and $||\overline{C'P'}|| \ll ||\overline{O_{Rn}C'}||$, we have $||\overline{O_{Tm}P'}|| \approx ||\overline{O_{Tm}P_1}||$ and $||\overline{O_{Rn}P'}|| \approx ||\overline{O_{Rn}P_2}||$, then it yields

$$R_P(t_m; m, n) \approx \left\|\overline{O_{Tm}P_1}\right\| + \left\|\overline{O_{Rn}P_2}\right\| \quad (10)$$
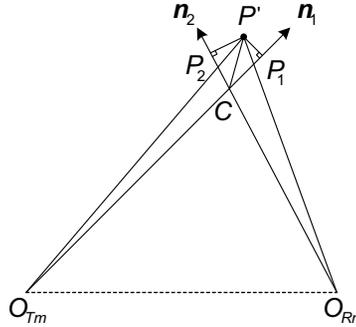
Figure 2. The simplified geometry of the target and a pair of transmitter and receiver.

When the scatterer P rotating around the center C, the geometry of the target at t_m is redrawn in Fig. 3 to deduce the expression of $R_\Delta(t_m; m, n)$. In Fig. 3, $\overline{C'P'}$ is the vector of the radius with length of r; $\mathbf{n}'_1$ and $\mathbf{n}'_2$ are the projections of $\mathbf{n}_1$ and $\mathbf{n}_2$ on the plane spanned by the trajectory of scatterer P' respectively; P_1 and P_2 are the projections of P' on $\mathbf{n}_1$ and $\mathbf{n}_2$ respectively. Assume that the included angle between $\overline{C'P'}$ and $\mathbf{n}'_1$ at t_m is Ωt_m and that the lengths of $\overline{C'P_1}$ and $\overline{C'P_2}$ (i.e., $||\overline{C'P_1}||$ and $||\overline{C'P_2}||$) are positive when $\overline{C'P_1}$
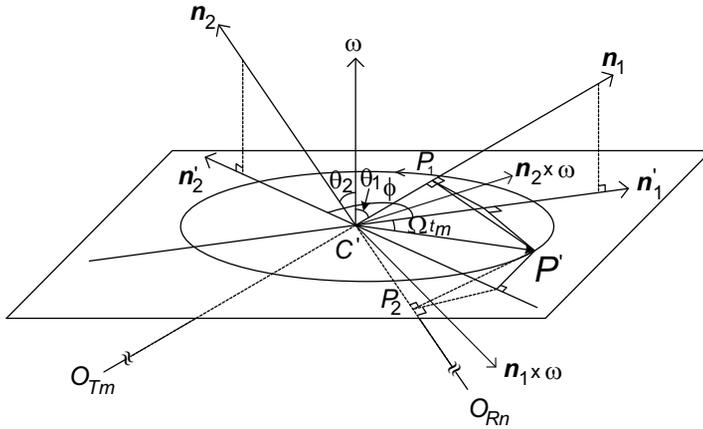
Figure 3. Geometry of the rotating target and a pair of transmitter and receiver.

and $\overline{C'P_2}$ have the same directions with $\mathbf{n}_1$ and $\mathbf{n}_2$, respectively, and vice versa. Then we have

$$
\begin{aligned}
\left\|\overline{C'P_1}\right\| &= \left\|\overline{C'P'}\right\| \cos(\Omega t_m) \sin\theta_1, \\
\left\|\overline{C'P_2}\right\| &= \left\|\overline{C'P'}\right\| \cos(\Omega t_m + \phi) \sin\theta_2
\end{aligned}
\tag{11}
$$

where θ_1 is the included angle between $\boldsymbol{\omega}$ and $\mathbf{n}_1$, θ_2 the included angle between $\boldsymbol{\omega}$ and $\mathbf{n}_2$, and ϕ the included angle between $\mathbf{n}_1'$ and $\mathbf{n}_2'$. Substitute (11) and (9) to (10) yields

$$
\begin{aligned}
R_P(t_m; m, n) &= \left(\left\|\overline{O_{Tm}C'}\right\| + \left\|\overline{C'P_1}\right\|\right) + \left(\left\|\overline{O_{Rn}C'}\right\| + \left\|\overline{C'P_2}\right\|\right) \\
&= \left(\left\|\overrightarrow{O_{Tm}o} + \overrightarrow{oC} + \mathbf{v}t_m\right\| + \left\|\overline{C'P_1}\right\|\right) + \left(\left\|\overrightarrow{O_{Rn}o} + \overrightarrow{oC} + \mathbf{v}t_m\right\| + \left\|\overline{C'P_2}\right\|\right) \\
&= R_C(0; m, n) + r\cos(\Omega t_m)\sin\theta_1 + r\cos(\Omega t_m + \phi)\sin\theta_2 \\
&\quad + \left(\begin{array}{c} \dfrac{(X_o - X_{Tm} + x_C)v_X + (Y_o - Y_{Tm} + y_C)v_Y + (Z_o - Z_{Tm} + z_C)v_Z}{\sqrt{(X_o - X_{Tm} + x_C)^2 + (Y_o - Y_{Tm} + y_C)^2 + (Z_o - Z_{Tm} + z_C)^2}} \\ + \dfrac{(X_o - X_{Rn} + x_C)v_X + (Y_o - Y_{Rn} + y_C)v_Y + (Z_o - Z_{Rn} + z_C)v_Z}{\sqrt{(X_o - X_{Rn} + x_C)^2 + (Y_o - Y_{Rn} + y_C)^2 + (Z_o - Z_{Rn} + z_C)^2}} \end{array}\right) t_m
\end{aligned}
\tag{12}
$$

Therefore, we have

$$
\begin{aligned}
R_\Delta(t_m; m, n) &= R_P(t_m; m, n) - R_0(t_m; m, n) \approx (R_C(0; m, n) - R_0(0; m, n)) \\
&\quad + \left(\begin{array}{c} \dfrac{x_C v_X + y_C v_Y + z_C v_Z}{\sqrt{(X_o - X_{Tm})^2 + (Y_o - Y_{Tm})^2 + (Z_o - Z_{Tm})^2}} \\ + \dfrac{x_C v_X + y_C v_Y + z_C v_Z}{\sqrt{(X_o - X_{Rn})^2 + (Y_o - Y_{Rn})^2 + (Z_o - Z_{Rn})^2}} \end{array}\right) t_m \\
&\quad + (r\cos(\Omega t_m)\sin\theta_1 + r\cos(\Omega t_m + \phi)\sin\theta_2) = p_1 + p_2 + p_3
\end{aligned}
\tag{13}
$$

From (13), it can be found that the expression of $R_\Delta(t_m; m, n)$ can be divided into three parts: the first part $(p_1 = R_C(0; m, n) - R_0(0; m, n))$ is a constant; the second part p_2 is a first order function with respect to t_m, which is induced by the movement of the target body; the last part p_3 is induced by the micromotion of P and can be rewritten as

$$p_3 = r\sqrt{\sin^2\theta_1 + \sin^2\theta_2 + 2\sin\theta_1\sin\theta_2\cos\phi} \cdot \sin(\Omega t_m - \varphi) \quad (14)$$

where $\varphi = \arctan\left((\sin\theta_1 + \sin\theta_2\cos\phi)/(\sin\theta_2\sin\phi)\right)$.

Assuming that the migration through range cell (MTRC) [27, 28] of C is absent, the value of p_2 is smaller than a range cell and (7) can be approximately expressed as

$$S_{m,n}(f, t_m) = \sigma_P(m, n)\, T_p \text{sinc}\left(T_p\left(f + \mu(p_1 + p_3)/c\right)\right)$$
$$\exp\left(-j2\pi\left(f_c/c + mk/(T_p c)\right)(p_1 + p_2 + p_3)\right) \quad (15)$$

From (15), it can be found that: on the $f - t_m$ plane determined by (15), after the range scaling by $f = -\mu\Delta R(t_m)/c$, the locations of peaks in a scatterer's profile appear as a sinusoidal curve with respect to t_m, and the period of the curve is equivalent to the rotation period. For a given value of f, taking the derivative of the phase term on the right side of (15) in terms of t_m and then the instantaneous frequency is obtained as

$$f_m(t_m) = -(f_c/c + mk/(T_p c))\left(\begin{array}{c}\frac{x_C v_X + y_C v_Y + z_C v_Z}{\sqrt{(X_o - X_{Tm})^2 + (Y_o - Y_{Tm})^2 + (Z_o - Z_{Tm})^2}} \\ + \frac{x_C v_X + y_C v_Y + z_C v_Z}{\sqrt{(X_o - X_{Rn})^2 + (Y_o - Y_{Rn})^2 + (Z_o - Z_{Rn})^2}}\end{array}\right)$$
$$-\left(\frac{f_c}{c} + \frac{mk}{T_p c}\right)\Omega r\sqrt{\sin^2\theta_1 + \sin^2\theta_2 + 2\sin\theta_1\sin\theta_2\cos\phi} \cdot \cos(\Omega t_m - \varphi) (16)$$

where the first term is the target body's Doppler frequency, and the second term is the micro-Doppler frequency induced by the micromotion.

From (15) and (16), three conclusions about the m-D effect in MIMO radar system can be obtained:

1) The m-D effect induced by the rotation appears as a sinusoidal curve on both the range-slow-time plane and the joint time-frequency plane, and the period of the curve is equivalent to the rotation period, which is similar to that in the monostatic radar system.

2) The amplitudes of the m-D curves on both the range-slow-time plane and the joint time-frequency plane are determined by r, θ_1, θ_2 and ϕ. Because the values of these four parameters varies when choosing different pairs of transmitter and receiver, the amplitudes also varies with respect to (m, n).

3) The initial phase φ of the m-D curves is determined by θ_1, θ_2 and ϕ, which means that it is difficult to determine the instantaneous

location of the rotating scatterer by extracting the initial phase feature of the m-D curve. However, in monostatic radar system, the phase of the m-D curve coincides with that of the motion equation of the rotating scatterer [11].

Figure 4 shows the comparison of the m-D curve obtained by a monostatic radar and a MIMO radar consisting of a pair of transmitter and a receiver. In the simulation, two transmitters are located at $(-3\,\text{km}, 0\,\text{km}, 0\,\text{km})$ (indexed as *Transmitter 1*) and $(5\,\text{km}, 0\,\text{km}, 0\,\text{km})$ (indexed as *Transmitter 2*) with carrier frequencies $10\,\text{GHz}$ and $11\,\text{GHz}$, respectively. The bandwidths of the transmitted signals are $600\,\text{MHz}$ with $T_p = 4\,\mu\text{s}$. A receiver is located at $(-3\,\text{km}, 0\,\text{km}, 0\,\text{km})$ which is the same as the location of *Transmitter 1*. Therefore, *Transmitter 1* and the receiver also simulate a monostatic radar. The initial location of the target center o is $(3\,\text{km}, 4\,\text{km}, 5\,\text{km})$. The translational velocity of the target is $\mathbf{v} = [100, 150, 100]^T\,\text{m/s}$. The coordinates of the rotation center C in the local coordinate system is $(1\,\text{m}, 1\,\text{m}, 1\,\text{m})$. A scatterer P rotates around C with angular velocity $\omega = [2\pi, 3\pi, 3\pi]^T\,\text{rad/s}$ and radius $r = 4.3716\,\text{m}$. Figs. 4(a) and (b) show the m-D curve on the range-slow-time plane obtained by the monostatic radar and the MIMO radar consisting of the pair of *Transmitter 2* and the receiver, respectively. It can be found that the amplitudes of the two m-D curves are different to each other. Moreover, none of the amplitudes of the two m-D curves equals the real rotation radius of the target, because the amplitudes of the m-D curves are

(a)   (b)
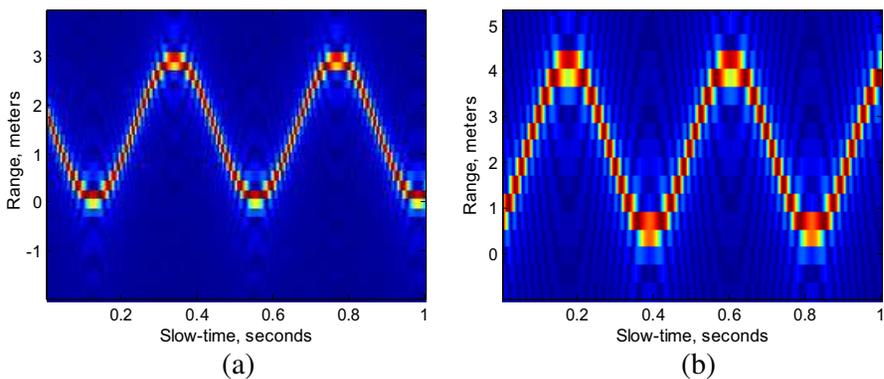
Figure 4. The comparison of the m-D curve obtained by (a) a monostatic radar and (b) a pair of a transmitter and a receiver in MIMO radar. The unit of the ordinate axis (f-axis) is transformed to meters by the range scaling $f = -2\mu\Delta R(t_m)/c$ and $f = -\mu\Delta R(t_m)/c$ respectively.

modulated by the LOS of the transmitters and the receiver. However, the periods of the m-D curves in Figs. 4(a) and (b) are the same as the period of the target's rotation, i.e., 0.4264 s, which will be useful to scatterer association if target contains multiple micromotions with different motion parameters (e.g., a helicopter with horizontal rotors and tail rotors).

3. THREE-DIMENSIONAL MICROMOTION SIGNATURE EXTRACTION

From the analyses in the last section, it can be found that when the MIMO radar system contains M transmitters and N receivers, MN m-D curves with different amplitudes corresponding to the same micromotional scatterer can be obtained. Because the amplitudes of m-D curves in MIMO radar are sensitive to r, θ_1, θ_2 and ϕ, it is possible to solve the value of r from the parameters of these MN m-D curves. In this section, the algorithm for m-D curves feature extraction is presented first and then the 3-D micromotion signature extraction method is outlined.

As mentioned in the last section, the m-D curves can be observed either on the $f - t_m$ plane or on the joint time-frequency plane. When the amplitude of the m-D curve is much larger than the range resolution, the m-D curve appears as a sinusoidal curve on the $f - t_m$ plane (or the range-slow-time plane), as shown in Fig. 4. In this case, the m-D curve spans several range cells and the magnitude of the curve is modulated by a sinc function as shown in (15). For a given value of f, it is generally difficult to observe a clear sinusoidal curve on the joint time-frequency plane because only limited number of segments of the m-D signal are used in time-frequency analysis, as shown in Fig. 5(a). Therefore, it will be better to extract the m-D features from the curves on the $f - t_m$ plane or the range-slow-time plane.

However, due to its sensitivity to the LOS, the amplitude of the m-D curve may be close to the range resolution or even smaller than the range resolution. As a result, the m-D curves on the $f - t_m$ plane will appears almost as straight lines, which makes feature extraction of the m-D curves, as shown in Fig. 5(b), difficult. In this case, since the value of p_3 is very small, we let $f = -\mu p_1/c$ (i.e., extract the straight line) and observe the m-D curves on the joint time-frequency plane. Limited by the resolution of the time-frequency analysis, it is difficult to obtain reasonably accurate feature parameters of the m-D curve, especially when several micromotional scatterers coexist within a range cell. So, it is necessary to develop a feature extraction algorithm to deal with these cases.
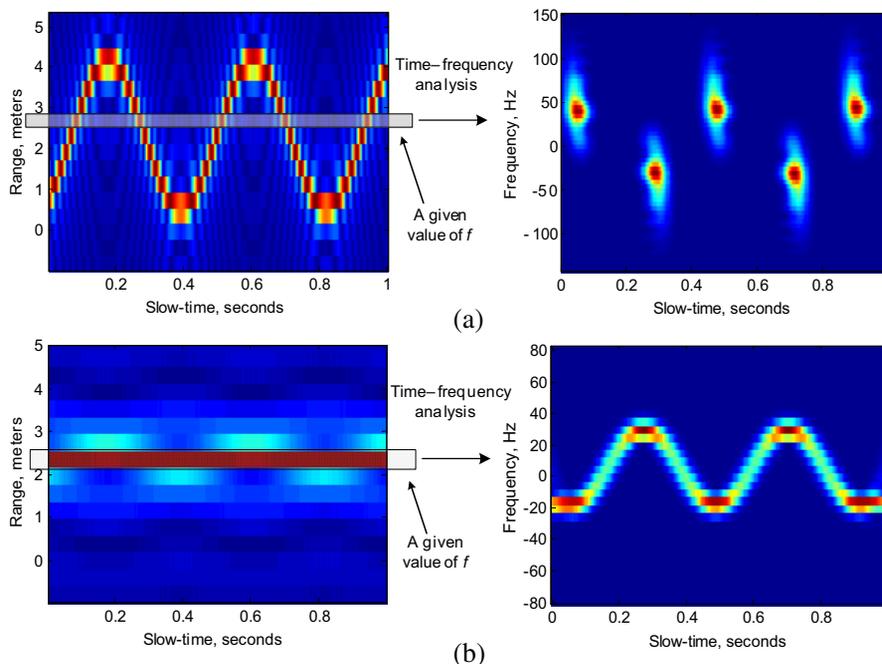
Figure 5. Time-frequency analysis of m-D signals. (a) Time-frequency analysis result of the m-D signal when the m-D curve amplitude is much larger than the range resolution. (b) Time-frequency analysis result of the m-D signal when the amplitude is close to the range resolution or even smaller than the range resolution.

The section presents the three steps in arriving at a new extraction algorithm: 1) m-D curve feature extraction on the range-slow-time plane; 2) feature extraction of m-D curve with small amplitude; and 3) 3-D micromotion signature extraction.

3.1. m-D Curve Feature Extraction on Range-slow-time Plane

According to (15), the m-D curve on the $f - t_m$ plane is expressed as

$$f = -\mu (p_1 + p_3)/c = -\mu (R_C (0; m, n) - R_0 (0; m, n))/c$$
$$-\frac{\mu}{c}r\sqrt{\sin^2\theta_1 + \sin^2\theta_2 + 2\sin\theta_1\sin\theta_2\cos\phi} \cdot \sin(\Omega t_m - \varphi) \quad (17)$$

After range scaling, the m-D curve on the range-slow-time plane can be rewritten as

$$
\begin{aligned}
R &= -cf/\mu = (R_C\,(0;m,n) - R_0\,(0;m,n)) \\
&\quad + r\sqrt{\sin^2\theta_1 + \sin^2\theta_2 + 2\sin\theta_1\sin\theta_2\cos\phi} \cdot \sin\left(\Omega t_m - \varphi\right) \\
&= d + A\sin\left(\Omega t_m - \varphi\right)
\end{aligned}
\tag{18}
$$

where $A = r\sqrt{\sin^2\theta_1 + \sin^2\theta_2 + 2\sin\theta_1\sin\theta_2\cos\phi}$ and $d = R_C(0;m,n) - R_0(0;m,n)$. It can be found that the m-D curve is determined by four parameters $(d,\,A,\,\Omega,\,\varphi)$. In order to obtain these parameters of the m-D curves, the Hough transform (HT) can be utilized to detect the sinusoids on the range-slow-time plane. Similar to the application of HT in [11], the m-D curve features can be extracted by HT with the four-parameter equation expressed by (18).

The rotating rate Ω of the micromotional scatterer can be obtained directly from the parameters detected by HT. However, the rotating radius r cannot be calculated from these parameters if only one pair of transmitter and receiver is utilized to analyze the m-D effect of the target.

3.2. Feature Extraction of m-D Curve With Small Amplitude

When the amplitude of the m-D curve is close to the range resolution or even smaller than the range resolution, the m-D curves on the range-slow-time plane will appears as straight lines. In this case, the Hough transform cannot extract the parameters of the micromotional scatterers. From (15), it can be found that if we let $f = -\mu p_1/c$ and extract the straight line, $S_{m,n}(f,\,t_m)$ can be rewritten as

$$
S'_{m,n}(t_m) = \sigma_P(m,n)T_p\exp\left(-j2\pi\left(\frac{f_c}{c} + \frac{mk}{T_p c}\right)(p_1 + p_2 + p_3)\right)
\tag{19}
$$

where the derivative of the phase term on the right side of (19) in terms of t_m is expressed in (16). Obviously, the time-frequency analysis can be utilized to transform the signal to time-frequency domain and then the HT can be used to detect the sinusoids on the joint time-frequency plane, which has been mentioned in [14]. However, in order to extract the 3-D micromotion signatures accurately, the parameters of m-D curves should be detected as close to their real values as possible. Limited by the resolution of the time-frequency analysis, the HT cannot obtain parameters of the curves with ideal precision. Moreover, when multiple micromotional scatterers coexist within a range cell, the mutual interference among the multi m-D

signals induced by these scatterers will blur the m-D curves on the joint time-frequency plane. As a result, the following HT processing may fail to detect the sinusoids. To deal with this problem, we design an m-D curve feature extraction algorithm based on the Orthogonal Matching Pursuit (OMP) algorithm.

As a refinement of the Matching Pursuit (MP) algorithm, the OMP algorithm is first developed by Pati et al. [29]. For a custom-built nonorthogonal and possibly overcomplete dictionary, by maintaining full backward orthogonality of the residual at every step (and thereby leads to improved convergence), OMP can give the optimal approximation of a signal with respect to the selected subset of the dictionary after a finite number of iterations. Due to this advantage, OMP in general converges faster than MP and performs well when the custom-built dictionaries are nonorthogonal [29, 30].

According to the basic idea of the OMP algorithm, we first build a dictionary and then implement OMP to decompose the m-D signals into a sum of selected atoms from the dictionary. From (16), it can be seen that $S'_{m,n}(t_m)$ is a sinusoidal frequency modulated (SFM) signal in fact. Therefore, the SFM atoms are chosen to construct the dictionary $\mathbf{D} = \{\mathbf{d}_i\}$ for OMP. The ith SFM atom $\mathbf{d}_i$ is of the form:

$$\mathbf{d}_i = \exp\left(-j2\pi f_{0i} t_m - j2\pi r'_i \sin\left(\Omega_i t_m - \varphi_i\right)\right) \qquad (20)$$

and then the power of each atom should be normalized:

$$\mathbf{d}_i \leftarrow \mathbf{d}_i / \|\mathbf{d}_i\| \qquad (21)$$

where f_{0i} is the carrier frequency within the prospective value scales $[f_{0\min}, f_{0\max}]$, r'_i is the modulation magnitude within $[r'_{\min}, r'_{\max}]$, Ω_i is the modulation frequency within $[\Omega_{\min}, \Omega_{\max}]$ and φ_i is the initial phase within $[\varphi_{\min}, \varphi_{\max}]$.

Let $\mathbf{S} = S'_{m,n}(t_m)$ and then the OMP is implemented to extract the m-D features as follows:

Step 1) Initialization: the residual $\mathbf{R}_{S0} = \mathbf{S}$, the index set $\varsigma_0 = [\ ]$, the subset of the selected atoms $\mathbf{D}_0 = \varnothing$, the matching atoms recorder matrix $\mathbf{\Pi}_0 = [\ ]$ and the iteration counter $g = 1$.

Step 2) Compute $\{\langle \mathbf{R}_{Sg-1}, \mathbf{d}_i \rangle ; \mathbf{d}_i \in \mathbf{D}\backslash\mathbf{D}_{g-1}\}$.

Step 3) Find $\mathbf{d}'_i \in \mathbf{D}\backslash\mathbf{D}_{g-1}$ such that

$$\left|\langle \mathbf{R}_{Sg-1}, \mathbf{d}'_i \rangle\right| \geq \alpha \sup_i \left|\langle \mathbf{R}_{Sg-1}, \mathbf{d}_i \rangle\right|$$

where $\mathbf{d}_i \in \mathbf{D}\backslash\mathbf{D}_{g-1}$ and $0 < \alpha \leq 1$.

Step 4) If $\left|\langle \mathbf{R}_{Sg-1}, \mathbf{d}'_i \rangle\right| < \delta$, where δ is a given power threshold and $\delta > 0$, stop.

Step 5) Record the index of $\mathbf{d}'_i$ in $\mathbf{D}$: $\varsigma_g = [\varsigma_{g-1} \ i']$; Update $\mathbf{D}_g = \mathbf{D}_{g-1} \cup \{\mathbf{d}'_i\}$ and $\mathbf{\Pi}_g = [\mathbf{\Pi}_{g-1}, \mathbf{d}'_i]$.

Step 6) Solve the optimization problem $\hat{\mathbf{x}} = \arg\min_x \|\mathbf{S} - \mathbf{\Pi}_g\mathbf{x}\|_2$, which yields $\hat{\mathbf{x}} = (\mathbf{\Pi}_g^H\mathbf{\Pi}_g)^{-1}\mathbf{\Pi}_g^H\mathbf{S}$ according to the least square method.

Step 7) Update $\mathbf{R}_{Sg} = \mathbf{S} - \mathbf{\Pi}_g\hat{\mathbf{x}}$ and $g \leftarrow g+1$. If $g \leq G$, where G is the predetermined maximum number of iterations, return to Step 2); if $g = G$, finish the iteration.

From the above algorithm, it can be found that the m-D signal $\mathbf{S}$ is approximately decomposed to the sum of the atoms in $\mathbf{D}_g$, i.e.,

$$S = \mathbf{\Pi}_g\hat{\mathbf{x}} + \mathbf{R}_{Sg} \tag{22}$$

The parameters $(f_{0i}, r'_i, \Omega_i, \varphi_i)$ of the atoms in $\mathbf{D}_g$ denote the m-D features:

$$r'_i = \left(\frac{f_c}{c} + \frac{mk}{T_pc}\right) r\sqrt{\sin^2\theta_1 + \sin^2\theta_2 + 2\sin\theta_1\sin\theta_2\cos\phi},$$
$$\Omega_i = \Omega, \quad \varphi_i = \varphi \tag{23}$$

3.3. 3-D Micromotion Signature Extraction Algorithm

Assume that the MIMO radar system contains M transmitters and N receivers, and then MN m-D curves corresponding to a micromotional scatterer can be obtained. If the amplitude of the m-D curve is larger than the range resolution, HT is utilized to extract the m-D features; otherwise, if the amplitude of the m-D curve is close to or even smaller than the range resolution, OMP is utilized. Assume h_1 m-D curves are processed by HT and the other $h_2 = MN - h_1$ m-D curves are processed by OMP, thus we can construct the following equation system

$$\begin{cases} A_i = r\sqrt{\sin^2\theta_{1i} + \sin^2\theta_{2i} + 2\sin\theta_{1i}\sin\theta_{2i}\cos\phi_i}, \\ \qquad\qquad\qquad\qquad\qquad\qquad i = 1, 2, \ldots, h_1 \\ r'_i = \left(\frac{f_c}{c} + \frac{mk}{T_pc}\right) r\sqrt{\sin^2\theta_{1i} + \sin^2\theta_{2i} + 2\sin\theta_{1i}\sin\theta_{2i}\cos\phi_i}, \\ \qquad\qquad\qquad\qquad\qquad\qquad i = 1, 2, \ldots, h_2 \end{cases} \tag{24}$$

Because θ_{1i} is the included angle between $\boldsymbol{\omega}$ and $\mathbf{n}_{1i}$, θ_{2i} is the included angle between $\boldsymbol{\omega}$ and $\mathbf{n}_{2i}$, it can be obtained

$$\theta_{1i} = \arccos\left(\frac{\boldsymbol{\omega}\cdot\mathbf{n}_{1i}}{|\boldsymbol{\omega}|\cdot|\mathbf{n}_{1i}|}\right), \ \ \theta_{2i} = \arccos\left(\frac{\boldsymbol{\omega}\cdot\mathbf{n}_{2i}}{|\boldsymbol{\omega}|\cdot|\mathbf{n}_{2i}|}\right), \ \ 0 \leq \theta_{1i}, \ \theta_{2i} \leq \pi \tag{25}$$

According to Fig. 3, when $0 \leq \phi_i \leq \pi$, ϕ_i equals to the included angle between the vector $\mathbf{n}_{1i} \times \boldsymbol{\omega}$ and $\mathbf{n}_{2i} \times \boldsymbol{\omega}$, i.e., $\phi_i = (\mathbf{n}_{1i} \times \boldsymbol{\omega}, \mathbf{n}_{2i} \times \boldsymbol{\omega})$; when $\pi \leq \phi_i \leq 2\pi$, it yields $\phi_i = 2\pi - (\mathbf{n}_1 \times \boldsymbol{\omega}, \mathbf{n}_2 \times \boldsymbol{\omega})$. Therefore, the term $\cos\phi_i$ in (24) can be calculated by

$$\cos\phi_i = (\mathbf{n}_{1i} \times \boldsymbol{\omega}) \cdot (\mathbf{n}_{2i} \times \boldsymbol{\omega})/(|\mathbf{n}_{1i} \times \boldsymbol{\omega}| \cdot |\mathbf{n}_{2i} \times \boldsymbol{\omega}|) \tag{26}$$

When the location of the target is known, $\mathbf{n}_{1i}$ and $\mathbf{n}_{2i}$ can be considered as known vectors. After the m-D curves feature extraction, A_i, r_i' and Ω are all known. Therefore, substituting (25) and (26) to (24), it can be found that the unknown parameters in (24) are $\boldsymbol{\omega} = [\omega_x, \omega_y, \omega_z]^T$ and r. Considering $\Omega = \|\boldsymbol{\omega}\|$, the multivariable equation system in (24) can be reconstructed as follows:

$$
\begin{cases}
A_i = r\sqrt{\sin^2\theta_{1i} + \sin^2\theta_{2i} + 2\sin\theta_{1i}\sin\theta_{2i}\cos\phi_i}, \\
\qquad\qquad\qquad\qquad\qquad\qquad i = 1, 2, \ldots, h_1 \\
r_i' = \left(\dfrac{f_c}{c} + \dfrac{mk}{T_p c}\right) r\sqrt{\sin^2\theta_{1i} + \sin^2\theta_{2i} + 2\sin\theta_{1i}\sin\theta_{2i}\cos\phi_i}, \\
\qquad\qquad\qquad\qquad\qquad\qquad i = 1, 2, \ldots, h_2 \\
\omega_x^2 + \omega_y^2 + \omega_z^2 = \Omega^2
\end{cases} \quad (27)
$$

where the unknown parameters to be solved are $(\omega_x, \omega_y, \omega_z, r)$. It is difficult to derive the analytical solution to this equation system. Therefore, numerical methods such as the Newton method and quasi-Newton method can be used to solve the approximate roots. Since there are four parameters to be solved, it must be satisfied that $MN \geq 3$ to solve the roots of (27). The accuracy of the solution can be further improved by increasing the number of equations for stricter constraints by utilizing more transmitters and receivers in the MIMO radar system.

After the parameters $(\omega_x, \omega_y, \omega_z, r)$ have been solved, the angular velocity of rotation $\boldsymbol{\omega}$ and the real radius of the rotation r can be obtained. Compared with the micromotion signatures obtained from monostatic radar systems, the MIMO radar systems can offer more precise 3-D m-D signatures.

4. SIMULATIONS

4.1. Effectiveness Validation

In the simulation, the MIMO radar contains 2 transmitters and 4 receivers. The two transmitters are located at $(0, 0, 0)$ km (indexed as $T1$) and $(30, 0, 0)$ km (indexed as $T2$) with carrier frequencies $10\,\text{GHz}$ and $11\,\text{GHz}$, respectively. The bandwidth of the transmitted signal is $600\,\text{MHz}$ and $T_p = 4\,\mu\text{s}$. The four receivers are located at $(-5, 0, 0)$ km (indexed as $R1$), $(30, -40, 0)$ km (indexed as $R2$), $(70, 0, 0)$ km (indexed as $R3$) and $(-40, -50, 0)$ km (indexed as $R4$), respectively. The pulse repetition frequency (PRF) is $1\,\text{KHz}$. The target model is shown in Fig. 6. The initial location of the target center o is $(20, 30,$
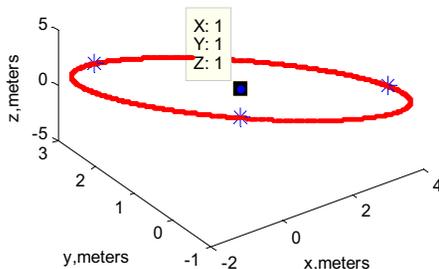
Figure 6. The geometry of the target with three rotating scatterers (each "*" denotes a rotating scatterer). The rotation center is located at (1 m, 1 m, 1 m) in the local coordinate system.

3) km in the global coordinate system and the translational velocity of the target is $\mathbf{v} = [100, 50, 0]^T$ m/s. The coordinates of the rotation center C in the local coordinate system are (1 m, 1 m, 1 m). Three scatterers rotate around C, and all of their angular velocities and radii are $\boldsymbol{\omega} = [2\pi, 3\pi, 0.3\pi]^T$ rad/s $= [6.2832, 9.4248, 0.9425]^T$ rad/s and $r = 3.3453$ m respectively. $\Omega = 11.3663$ rad/s.

The obtained m-D curves on the range-slow-time plane of each pair of transmitter (T) and receiver (R) are shown in Table 1. The amplitudes of the m-D curves obtained by different pairs of T/R have different values. The amplitudes of the m-D curves obtained

Table 1. The m-D curves on the range-slow-time plane of each pair of T/R.

by $(T1, R1)$ and $(T1, R4)$ are small such that they appear as straight lines, whereas the amplitudes of the m-D curves obtained by the other pairs of T/R are relatively large. Therefore, the m-D curves feature extractions of $(T1, R1)$ and $(T1, R4)$ are implemented by the OMP algorithm, and the others are implemented by HT.

Taking the returns from $(T1, R1)$ for example, OMP is utilized to extract the m-D curves features and the results are shown in Table 2. It can be seen that the power coefficients of the atoms are decreasing with respect to the iteration number, which demonstrates the convergence of the algorithm. The power coefficients of the first three atoms are much larger than the fourth one, which means that the first three atoms are corresponding to the m-D signals of the three rotation scatterers. According to (23), the theoretical value of r_i' can be calculated as 1.8000, which is close to the values in the table. Besides, the values of Ω_i in the table are also close to the theoretical value $\Omega = 11.3663\,\mathrm{rad/s}$.

Similarly, the m-D curves feature extraction results of $(T1, R4)$ by OMP are $\Omega_i = 11.3620$ and $r_i' = 9.3333$, which are close to the theoretical value $\Omega = 11.3663\,\mathrm{rad/s}$ and $r_i' = 9.1167$ according to (23).

Table 2. m-D curves feature extraction results of $(T1, R1)$ obtained by the OMP algorithm.

Iteration number	f_{0i}	r_i'	Ω_i	φ_i	Power coefficient $(\hat{x})$
1	-1.0000	1.8000	11.3826	0.0500	6547.4
2	-1.0000	1.8000	11.4032	4.2500	6438.7
3	-1.0000	1.8333	11.4032	2.2000	6255.5
4	9.0000	2.0000	11.2200	2.6500	1910.0

The features of m-D curves obtained by other pairs of T/R are extracted by HT, and the results are shown in Table 3. The values of Ω in the table are close to the theoretical value $11.3663\,\mathrm{rad/s}$, and the values of A in different pairs of T/R are different from each other. According to (18), the theoretical values of A in $(T1, R2)$, $(T1, R3)$, $(T2, R1)$, $(T2, R2)$, $(T2, R3)$ and $(T2, R4)$ can be calculated as 2.6393, 3.7542, 2.2737, 4.8549, 5.9729 and 2.4410 respectively, which are close to the HT results shown in the table.

Because Ω is insensitive to the LOS of the T/R pairs, the precision of the extracted value of Ω can be improved by calculating the average value of all obtained Ω_i in Tables 2, 3, which yields $\bar{\Omega} = 11.36\,\mathrm{rad/s}$. Let $\Omega \leftarrow \bar{\Omega}$ and substitute A_i and r_i' into (27), then $(\omega_x, \omega_y, \omega_z, r)$ can

Table 3. m-D curves feature extraction results obtained by HT.

Pairs of T/R	Index of m-D curves	d_i	A_i	Ω_i	φ_i
$(T1, R2)$	1	1.7910	2.6866	11.3620	1.0000
	2	1.7910	2.6866	11.3826	3.1000
	3	1.7910	2.6866	11.3620	5.2000
$(T1, R3)$	1	0.4800	3.8400	11.3620	1.0000
	2	0.4800	3.8400	11.3826	3.1000
	3	0.4800	3.8400	11.3415	5.1000
$(T2, R1)$	1	1.7910	2.2388	11.3620	0.9000
	2	1.7910	2.2388	11.4032	3.0000
	3	1.7910	2.2388	11.3620	5.1000
$(T2, R2)$	1	0.9449	4.7244	11.4240	1.0000
	2	0.9449	4.7244	11.3620	3.1000
	3	0.9449	4.7244	11.4032	5.2000
$(T2, R3)$	1	0.0000	5.9524	11.3620	1.0000
	2	0.0000	5.9524	11.3620	3.1000
	3	0.0000	5.9524	11.3620	5.2000
$(T2, R4)$	1	1.8045	2.2556	11.3620	0.9000
	2	1.8045	2.2556	11.3211	3.0000
	3	1.8045	2.2556	11.2804	5.2000

be resolved as (6.2185, 9.4508, 1.0348, 3.3222) by using the command *fsolve* in MATLAB, which are close to the true values.

4.2. Robustness Analysis

The precision of the obtained 3-D m-D signatures is mainly determined by two aspects: 1) because the 3-D m-D signatures are solved from the m-D curve features extracted by HT or OMP algorithm, the performance of HT and OMP will affect the precision of the 3-D m-D signatures; and 2) even if the HT and OMP algorithm works very well, the accuracy of the extracted m-D curve features is limited by the radar resolution, therefore, errors cannot be avoided when solving the 3-D m-D signatures. Hence, the robustness analysis of the proposed method consists of two parts: one is the robustness analysis of the m-D curve feature extraction, and the other is the robustness analysis of the 3-D m-D signature solution.

4.2.1. Robustness Analysis of the m-D Curve Feature Extraction

The robustness analysis of HT in the application of m-D curve feature extraction has been presented in our previous work [11], where the simulations demonstrated that HT is well functional when the signal-to-noise ratio (SNR) is higher than -5 dB. In this paper, we mainly carry out simulations to analyze the robustness of the OMP algorithm for feature extraction of the m-D curves with small amplitudes.

Similar to the simulations in [11], the complex Gaussian white noise is added to the returned signal. To simplify the analysis, we assume that a target of a point scatterer with rotation is illuminated by the MIMO radar. The simulation parameters of the MIMO radar and target's motion are the same as those in Section 4.1, and the returns of $(T1, R1)$ are chosen to analyze the robustness of the OMP algorithm. We define the error as

$$\rho = \hat{X} - X \tag{28}$$

where X denotes the true value of f_0, r', Ω and φ, $\hat{X}$ the corresponding estimated value, and $|\rho|$ the absolute error. Fig. 7 shows the absolute errors of the m-D curve parameters obtained by OMP while SNR changes from -20 dB to -50 dB. It can be seen that when SNR > -42 dB, the OMP algorithm can obtain precise parameters in the present case. It indicates that the OMP algorithm has better anti-noise ability than HT for the m-D curve feature extraction. This conclusion can be explained as follows: (1) the noise is distributed in the entire range-slow-time plane, whereas the m-D signal is mainly distributed in the range cell extracted to implement OMP algorithm. As a result, the effect of the noise on the algorithm is suppressed; (2) both the phases
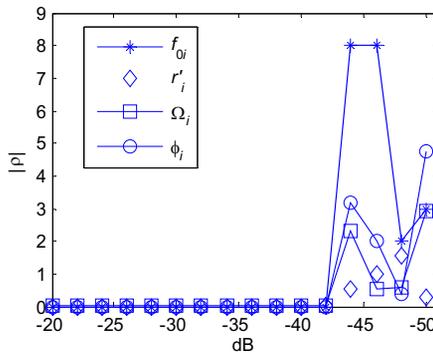
Figure 7. The absolute errors of the m-D curve parameters obtained by OMP when SNR changes from -20 dB to -50 dB.

and moduli of the m-D signal are used in the OMP algorithm, while only the moduli of the m-D signal are used in HT. Therefore, the OMP algorithm possesses better anti-noise ability when extracting the m-D curve features.

4.2.2. Robustness Analysis of the 3-D m-D Signature Solution

Limited by the radar resolution, the errors of the m-D curve parameters obtained by HT or OMP are inevitable. According to (27), A_i, r_i' and Ω are utilized to solve the three-dimensional m-D signatures. To analyze the influence of the estimation errors of A_i, r_i' and Ω on the three-dimensional m-D signature solution, we define the normalized error as

$$\rho' = \rho/X \tag{29}$$

and $|\rho'|$ denotes the normalized absolute error.

Without loss of generality, assume that the errors obey the Gaussian distribution. The Monte-carlo method is utilized to analyze the robustness of 3-D m-D signature solution, where 100 simulations are carried out in each following situation:

(i) Assuming that Ω is estimated precisely and that the estimations of A_i and r_i' are unbiased estimations (i.e., $E(\rho'_{A_i}) = 0$ and $E(\rho'_{r_i'}) = 0$), we investigate the relationship between the normalized absolute errors of the solved $(\omega_x, \omega_y, \omega_z, r)$ and the variance of ρ'_{A_i} and $\rho'_{r_i'}$ (i.e., $D(\rho'_{A_i})$ and $D(\rho'_{r_i'})$). Fig. 8(a) shows the curves of the normalized absolute errors of $(\omega_x, \omega_y, \omega_z, r)$ when both $D(\rho'_{A_i})$ and $D(\rho'_{r_i'})$ change from 0 to 0.5. It can be found that the normalized absolute errors of $(\omega_x, \omega_y, \omega_z, r)$ is linear with $D(\rho'_{A_i})$ and $D(\rho'_{r_i'})$ approximately.

(ii) Assume that Ω is estimated precisely and that the estimations of A_i and r_i' are biased estimations (i.e., $E(\rho'_{A_i}) \neq 0$ and $E(\rho'_{r_i'}) \neq 0$). For given $D(\rho'_{A_i})$ and $D(\rho'_{r_i'})$, we investigate the relationship between the normalized absolute errors of $(\omega_x, \omega_y, \omega_z, r)$ and the mathematical expectation of ρ'_{A_i} and $\rho'_{r_i'}$ (i.e., $E(\rho'_{A_i})$ and $E(\rho'_{r_i'})$). Fig. 8(b) shows the curves of the normalized absolute errors of $(\omega_x, \omega_y, \omega_z, r)$ when $D(\rho'_{A_i}) = D(\rho'_{r_i'}) = 0.01$, $E(\rho'_{A_i})$ and $E(\rho'_{r_i'})$ change from -0.3 to 0.3. It can be found that the normalized absolute errors of r is linear with $|E(\rho'_{A_i})|$ and $|E(\rho'_{r_i'})|$ approximately, while the normalized absolute errors of $(\omega_x, \omega_y, \omega_z)$ are nearly independent to $E(\rho'_{A_i})$ and $E(\rho'_{r_i'})$. It indicates that the influence of $E(\rho'_{A_i})$ and $E(\rho'_{r_i'})$ on the solutions of

$(\omega_x, \omega_y, \omega_z)$ is weaker than that of $D(\rho'_{A_i})$ and $D(\rho'_{r'_i})$.

(iii) Assuming that both A_i and r'_i are estimated precisely, we investigate the relationship between the normalized absolute errors of $(\omega_x, \omega_y, \omega_z, r)$ and the normalized error of Ω (i.e., ρ'_Ω). Fig. 8(c) shows the curves of the normalized absolute errors of $(\omega_x, \omega_y, \omega_z, r)$ when ρ'_Ω changes from -0.3 to 0.3. It can be found that the normalized absolute errors of r are close to zero, while the normalized absolute errors of $(\omega_x, \omega_y, \omega_z)$ are linear with $|\rho'_\Omega|$. This phenomenon can be explained as follows: in (27), the values of A_i and r'_i are determined by r, θ_1, θ_2 and ϕ. Because the values of θ_1, θ_2 and ϕ are related to the direction of $\boldsymbol{\omega} = [\omega_x, \omega_y, \omega_z]^T$ and independent to the Ω, the
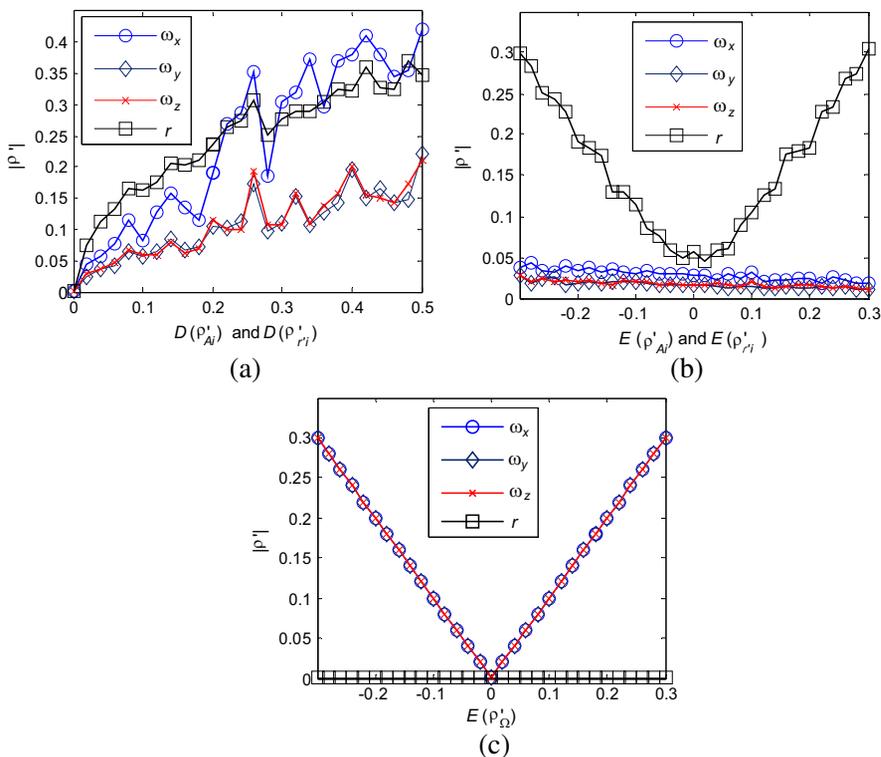

Figure 8. Robustness analysis of the three-dimensional m-D signature solution. (a) Ω is estimated precisely, $E\left(\rho'_{A_i}\right) = 0$ and $E\left(\rho'_{r'_i}\right) = 0$. (b) Ω is estimated precisely, $D\left(\rho'_{A_i}\right) = D\left(\rho'_{r'_i}\right) = 0.01$. (c) A_i and r'_i are estimated precisely.

estimation precision of Ω doesn't affect the solution of r. Whereas according to $\omega_x^2 + \omega_y^2 + \omega_z^2 = \Omega^2$, when $|\rho'_\Omega|$ increasing linearly, the normalized absolute errors of $(\omega_x, \omega_y, \omega_z)$ will also increase linearly.

In practice, the estimation of Ω can be improved by averaging the Ω_i extracted from all pairs of transmitter and receiver. In this case, the errors of Ω are usually negligible. When SNR > -5 dB, both the HT and OMP algorithm can obtain the m-D curve features with high precision. Therefore, the 3-D m-D signatures can be obtained successfully.

4.3. Helicopter Simulation

In the following simulation, we choose a helicopter model to validate the effectiveness of the proposed method. The prototype of the scattering model is the AS350 helicopter of Eurocopter Company. Fig. 9 shows the framework of the AS350 and the corresponding scattering model. The helicopter contains three main rotors and two tail rotors. The main rotor rotates with frequency of 394 r/min (i.e., $\Omega_{main} = 41.2596$ rad/s), angular velocity of $\boldsymbol{\omega}_{main} = [0, 0, 41.2596]^T$ rad/s and radius of $r_{main} = 5.3450$ m. The tail rotor rotates with frequency of 2086 r/min (i.e., $\Omega_{tail} = 218.4454$ rad/s), angular velocity of $\boldsymbol{\omega}_{tail} = [0, 218.4454, 0]^T$ rad/s and radius of $r_{tail} = 0.93$ m. The centre of the target is located at (20 km, 30 km, 3 km) in the global coordinate system. The translational velocity of the target is $\mathbf{v} = [50, 50, 0]^T$ m/s. Assume each rotor blade contains one scatterer located on its tip, and that the situation whereby rotor scatterers are obstructed by the helicopter body is not considered. The location of the transmitters and receivers are the same as the simulation in Section 4.1. The carrier frequencies of the two transmitters are 4 GHz and 5 GHz respectively. The bandwidth of the transmitted signal is


(a)   (b)
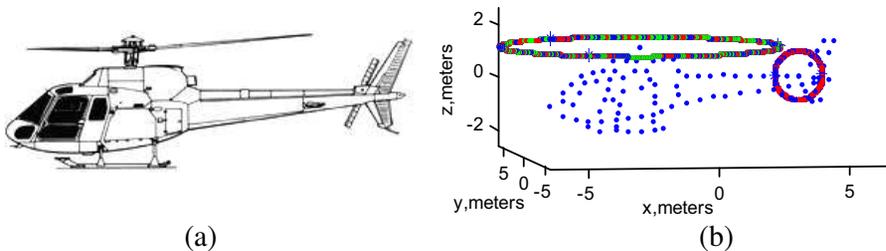
Figure 9. The helicopter target model. (a) The framework for the AS 350 of Eurocopter company. (b) The scattering model.

300 MHz and $T_p = 4\,\mu s$. 0 dB complex Gaussian white noise is added to the returned signal.

The helicopter echoes on the $f - t_m$ plane of each pair of T/R are shown in Table 4. The HT and OMP algorithm are implemented to extract the m-D curve features of the main rotors and tail rotors respectively, and the results are shown in Tables 5 and 6 respectively. It can be calculated that $\bar{\Omega}_{main} = 41.2323\,\text{rad/s}$ and $\bar{\Omega}_{tail} = 218.0837\,\text{rad/s}$, which are very close to the true values. From the m-D curve features, the 3-D micromotion signatures of the main rotor and tail rotor are solved as $(\omega_x,\ \omega_y,\ \omega_z,\ r)=(3.0011, 0.0539, 40.7932, 5.3896)$ and $(\omega_x,\ \omega_y,\ \omega_z,\ r) =$

Table 4. The echoes of the helicopter on the range-slow-time plane of each pair of T/R.
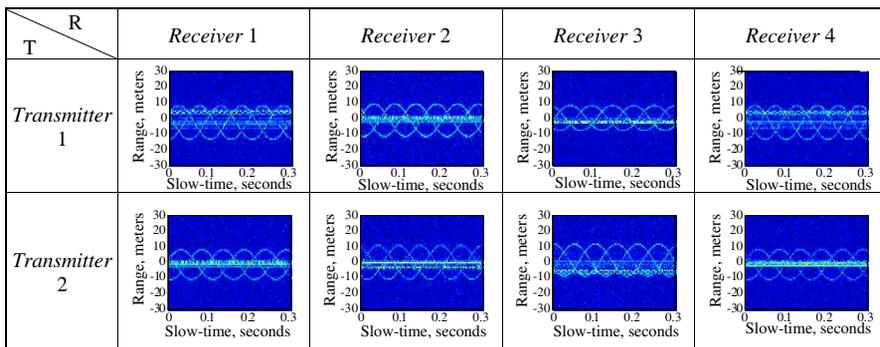
Table 5. The m-D curve features of main rotors obtained by HT.

R﹨T	Receiver 1	Receiver 2
Transmitter 1	$A_i = 10.5905$ $\Omega_i = 41.2824$	$A_i = 10.2975$ $\Omega_i = 41.0934$
Transmitter 2	$A_i = 9.4050$ $\Omega_i = 41.2596$	$A_i = 10.6150$ $\Omega_i = 41.2824$
R﹨T	Receiver 3	Receiver 4
Transmitter 1	$A_i = 7.9690$ $\Omega_i = 41.2283$	$A_i = 10.5905$ $\Omega_i = 41.3367$
Transmitter 2	$A_i = 10.1600$ $\Omega_i = 41.2283$	$A_i = 9.4050$ $\Omega_i = 41.1473$

Table 6. The m-D curve features of tail rotors obtained by OMP.

R T	Receiver 1	Receiver 2
Transmitter 1	$r_i' = 13.6125$ $\Omega_i = 216.6616$	$r_i' = 4.1250$ $\Omega_i = 217.4113$
Transmitter 2	$r_i' = 5.7005$ $\Omega_i = 220.4626$	$r_i' = 7.3785$ $\Omega_i = 216.6616$
R T	Receiver 3	Receiver 4
Transmitter 1	$r_i' = 5.3860$ $\Omega_i = 220.4626$	$r_i' = 13.0555$ $\Omega_i = 218.9263$
Transmitter 2	$r_i' = 18.2900$ $\Omega_i = 218.1662$	$r_i' = 4.8480$ $\Omega_i = 215.9170$

$(-0.7451, 217.2934, 2.7887, 0.9559)$ respectively, which are close to the predesigned values. It demonstrates that the proposed method can obtain the 3-D micromotion signatures accurately.

5. CONCLUSION

The micromotion signatures are very useful for radar target recognition. In monostatic radars, only the micromotion signatures projected onto the LOS could be extracted from the target's echoes. To obtain the full micromotion signatures of radar targets, a method for extracting the 3-D micromotion signatures is proposed in the paper. By taking advantage of the multi-view of MIMO radar, the 3-D micromotion signatures, such as the radius of a rotating object and the angular velocity vector of rotation, which are very important to automatic target recognition, can be obtained. Although only the rotational micromotion is taken into account in this paper, the proposed algorithm can be extended to obtain the 3-D micromotion signatures of other kinds of micromotion dynamics, such as vibration and precession.

Moreover, based on the 3-D micromotion signatures, it is possible to further obtain the 3-D ISAR image of the target. Different from the conventional 2-D ISAR imaging techniques, this kind of 3-D ISAR image can indicate the true size of the target, which can provide more precise information for target recognition. In our future work, we will take in-depth research on the 3-D ISAR imaging techniques for micromotional targets.

REFERENCES

1. Chen, V. C., F. Li, S. S. Ho, and H. Wechsler, "Micro-Doppler effect in radar: Phenomenon, model and simulation study," *IEEE Trans. on Aerosp. Electron. Syst.*, Vol. 42, No. 1, 2–21. Jan. 2006.

2. Guo, K. Y. and X. Q. Sheng, "A precise recognition approach of ballistic missile warhead and decoy," *Journal of Electromagnetic Waves and Applications*, Vol. 23, Nos. 14–15, 1867–1875, 2009.

3. Pan, X. Y., W. Wang, J. Liu, D. J. Feng, Y. C. Liu, and G. Y. Wang, "Features extraction of rotationally symmetric ballistic targets based on micro-Doppler," *Progress In Electromagnetics Research*, Vol. 137, 727–740, 2013.

4. Park, J.-H. and N.-H. Myung, "Effective reconstruction of the rotation-induced micro-Doppler from a noise-corrupted signature," *Progress In Electromagnetics Research*, Vol. 138, 499–518, 2013.

5. Lim, H., J. H. Yoo, C. H. Kim, K. I. Kwon, and N. H. Myung, "Radar cross section measurement of a realistic jet engine structure with rotating parts," *Journal of Electromagnetic Waves and Applications*, Vol. 25, No. 7, 999–108, 2011.

6. Lei, P., J. P. Sun, J. Wang, and W. Hong, "Micromotion parameter estimation of free rigid targets based on radar micro-Doppler," *IEEE Trans. on Geosci. Remote Sens.*, Vol. 50, No. 10, 3776–3786, 2012.

7. Lim, H., J. H. Park, J. H. Yoo, C. H. Kim, K. I. Kwon, and N. H. Myung, "Joint time-frequency analysis of radar micro-Doppler signatures from aircraft engine models," *Journal of Electromagnetic Waves and Applications*, Vol. 25, Nos. 8–9, 1069–1080, 2011.

8. Han, S. K., H. T. Kim, S. H. Park, and K. T. Kim, "Efficient radar target recognition using a combination of range profile and time-frequency analysis," *Progress In Electromagnetics Research*, Vol. 108, 131–140, 2010.

9. Park, J. H., H. Lim, and N. H. Myung, "Modified Hilbert-Huang transform and its application to measured micro Doppler signatures from realistic jet engine models," *Progress In Electromagnetics Research*, Vol. 126, 255–268, 2012.

10. Bai, X., M. Xing, F. Zhou, G. Lu, and Z. Bao, "Imaging of micromotion targets with rotating parts based on empirical-mode decomposition," *IEEE Trans. on Geosci. Remote Sens.*, Vol. 46, No. 11, 3514–3523, Nov. 2008.

11. Zhang, Q., T. S. Yeo, H. S. Tan, and Y. Luo, "Imaging of a moving target with rotating parts based on the Hough transform," *IEEE Trans. on Geosci. Remote Sens.*, Vol. 46, No. 1, 291–299, Jan. 2008.

12. Sparr, T. and B. Krane, "Micro-Doppler analysis of vibrating targets in SAR," *IEE Proc. — Radar Sonar Navig.*, Vol. 150, No. 4, 277–283, Aug. 2003.

13. Li, X., B. Deng, Y. L. Qin, H. Q. Wang, and Y. P. Li, "The influence of target micromotion on SAR and GMTI," *IEEE Trans. on Geosci. Remote Sens.*, Vol. 49, No. 7, 2738–2751, Jul. 2011.

14. Luo, Y., Q. Zhang, C.-W. Qiu, et al., "Micro-Doppler effect analysis and feature extraction in ISAR imaging with stepped-frequency chirp signals," *IEEE Trans. on Geosci. Remote Sens.*, Vol. 48, No. 4, 2087–2098, Apr. 2010.

15. Fishler, E., A. Haimovich, R. Blum, L. Cimini, D. Chizhik, and R. Valenzuela, "MIMO radar: An idea whose time has come," *Proceeding of the IEEE Radar Conference*, 71–78, Philadelphia, PA, 2004.

16. Qu, Y., G. S. Liao, S. Q. Zhu, X. Y. Liu, and H. Jiang, "Performance analysis of beamforming for MIMO radar," *Progress In Electromagnetics Research*, Vol. 84, 123–134, 2008.

17. Zhou, W., J. T. Wang, H. W. Chen, and X. Li, "Signal model and moving target detection based on MIMO synthetic aperture radar," *Progress In Electromagnetics Research*, Vol. 131, 311–329, 2012.

18. Hatam, M., A. Sheikhi, and M. A. Masnadi-Shirazi, "Target detection in pulse-train MIMO radars applying ICA algorithms," *Progress In Electromagnetics Research*, Vol. 122, 413–435, 2012.

19. Pastina, D., M. Bucciarelli, and P. Lombardo, "Multistatic and MIMO distributed ISAR for enhanced cross-range resolution of rotating targets," *IEEE Trans. on Geosci. Remote Sens.*, Vol. 48, No. 8, 3300–3317, Aug. 2010.

20. Zhu, Y. T., Y. Su, and W. X. Yu, "An ISAR imaging method based on MIMO technique," *IEEE Trans. on Geosci. Remote Sens.*, Vol. 48, No. 8, 3290–3299, Aug. 2010.

21. Wang, D.-W., X.-Y. Ma, A. L. Chen, and Y. Su, "High-resolution imaging using a wideband MIMO radar system with two

distributed arrays," *IEEE Trans. on Image Processing*, Vol. 19, No. 5, 1280–1289, May 2010.

22. Luo, Y., J. He, X.-J. Liang, and Q. Zhang, "Three-dimensional micro-Doppler signature extraction in MIMO radar," *The 2nd International Conference on Signal Processing Systems (ICSPS 2010)*, Vol. 2, 1–4, Dalian, China, Jul. 5–7, 2010.

23. Cheng, F., Z. S. He, H. M. Liu, et al., "The parameter setting problem of signal OFDM-LFM for MIMO radar," *International Conference on Communications, Circuits and Systems*, 876–880, Fujian, China, 2008.

24. Luo, Y., Q. Zhang, Y.-Q. Bai, et al., "High-resolution ISAR imaging with sparse-spectrum OFDM-LFM waveforms," *PIERS Proceedings*, 230–234, Kuala Lumpur, Malaysia, Mar. 2012.

25. Sen, S. and A. Nehorai, "OFDM MIMO radar with mutual-information waveform design for low-grazing angle tracking," *IEEE Trans. on Signal Processing*, Vol. 58, No. 6, 3152–3162, Jun. 2010.

26. Lin, Q. Q., P. F. Tang, B. Yuan, and Z. P. Chen, "A new dechirp method for wideband radar direct IF sampling signal," *2012 IEEE 11th International Conference on Signal Processing (ICSP)*, Vol. 3, 192–1924, 2012.

27. Kirkland, D. M., "An alternative range migration correction algorithm for focusing moving targets," *Progress In Electromagnetics Research*, Vol. 131, 227–241, 2012.

28. Zhang, L., T. Su, Z. Liu, and X. He, "High resolution ISAR imaging in receiver centered region area in bistatic radar," *EURASIP Journal on Advances in Signal Processing*, Vol. 50, 1–10, 2013.

29. Pati, Y. C., R. Rezaiifar, and P. S. Krishnaprasad, "Orthogonal matching pursuit: Recursive function approximation with applications to wavelet decomposition," *Proc. 27th Annu. Asilomar Conf. Signals, Systems, and Computers*, Vol. 1, 40–44, Pacific Grove, CA, Nov. 1993.

30. Tropp, J. A. and A. C. Gilbert, "Signal recovery from random measurements via orthogonal matching pursuit," *IEEE Trans. on Information Theory*, Vol. 53, No. 12, 4655–4666, Dec. 2007.